Article

# Frequency combs induced by phase turbulence

https://doi.org/10.1038/s41586-020-2386-6

Received: 9 November 2019

Accepted: 18 March 2020

Published online: 17 June 2020

Check for updates

Marco Piccardo[1,2,8]✉, Benedikt Schwarz[1,3,8], Dmitry Kazakov[1], Maximilian Beiser[3], Nikola Opačak[3], Yongrui Wang[4], Shantanu Jha[1,5], Johannes Hillbrand[1,3], Michele Tamagnone[1], Wei Ting Chen[1], Alexander Y. Zhu[1], Lorenzo L. Columbo[6,7], Alexey Belyanin[4] & Federico Capasso[1]✉

Wave instability—the process that gives rise to turbulence in hydrodynamics[1]—represents the mechanism by which a small disturbance in a wave grows in amplitude owing to nonlinear interactions. In photonics, wave instabilities result in modulated light waveforms that can become periodic in the presence of coherent locking mechanisms. These periodic optical waveforms are known as optical frequency combs[2–4]. In ring microresonator combs[5,6], an injected monochromatic wave becomes destabilized by the interplay between the resonator dispersion and the Kerr nonlinearity of the constituent crystal. By contrast, in ring lasers instabilities are considered to occur only under extreme pumping conditions[7,8]. Here we show that, despite this notion, semiconductor ring lasers with ultrafast gain recovery[9,10] can enter frequency comb regimes at low pumping levels owing to phase turbulence[11]—an instability known to occur in hydrodynamics, superconductors and Bose–Einstein condensates. This instability arises from the phase–amplitude coupling of the laser field provided by linewidth enhancement[12], which produces the needed interplay of dispersive and nonlinear effects. We formulate the instability condition in the framework of the Ginzburg–Landau formalism[11]. The localized structures that we observe share several properties with dissipative Kerr solitons, providing a first step towards connecting semiconductor ring lasers and microresonator frequency combs[13].

Following decades of studies, the development of optical frequency combs continues at a rapid pace[4,6,14]. Research on frequency combs started from tabletop optical systems—such as Ti:sapphire mode-locked lasers, which revolutionized optical metrology[2]—the subsequent advances in the processing of semiconductor and dielectric materials led to much more compact frequency comb generators. Technological progress went hand in hand with many new applications, such as in spectroscopy and chemical sensing, arbitrary radiofrequency waveform generation, optical communications and quantum information. Within the realm of integrated optics, of particular interest are two classes of generators: semiconductor lasers and passive microresonators[6,15]; in the latter, the pump is an external continuous-wave laser and the gain stems from the Kerr nonlinearity. In both cases, the device starts from single-frequency operation, corresponding to the first lasing mode or the external pump. To generate a frequency comb, mechanisms capable of creating modes at different frequencies, coupling them and locking their phases need to be present in the cavity. In microresonators, above the parametric instability threshold, the external pump induces the appearance of sidebands, which grow and proliferate[16] through cascaded parametric processes. This coherent nonlinear process gives rise to phase-locked frequency combs. In Fabry–Pérot semiconductor lasers, multimode operation results from inhomogeneous gain saturation. A standing wave created by the first lasing mode (Fig. 1a) leads to a spatially varying distribution of the gain—a phenomenon known as spatial hole burning (SHB). In a dispersive cavity, SHB leads to the proliferation of modes with nonequidistant frequencies, where phase locking can be achieved through the nonlinearity of the gain medium itself[17–20].

SHB is not expected to form in a ring cavity, as the clockwise and counterclockwise modes of a ring resonator are not naturally coupled in the absence of a well defined reflection point that breaks the circular symmetry. We show that semiconductor ring lasers[21–23] can nevertheless undergo a single-mode instability owing to a phenomenon known in the realm of the Ginzburg–Landau theory as phase turbulence[11] and form frequency combs even in the absence of spatial or spectral hole burning. Multimode emission and comb formation occur at a pumping level fractionally higher than the lasing threshold. This is in contrast to the Risken–Nummedal–Graham–Haken instability, which also promotes multimode operation of a ring laser but at a non-practical pumping level of at least nine times above the threshold[7,8].

## Ring frequency combs

To study phase turbulence in lasers, we use ring quantum cascade lasers (QCLs)[9]. These are monolithic frequency comb generators that

[1]Harvard John A. Paulson School of Engineering and Applied Sciences, Harvard University, Cambridge, MA, USA. [2]Center for Nano Science and Technology, Fondazione Istituto Italiano di Tecnologia, Milan, Italy. [3]Institute of Solid State Electronics, TU Wien, Vienna, Austria. [4]Department of Physics and Astronomy, Texas A&M University, College Station, TX, USA. [5]Physics Department, Yale University, New Haven, CT, USA. [6]Dipartimento di Elettronica e Telecomunicazioni, Politecnico di Torino, Turin, Italy. [7]Consiglio Nazionale delle Ricerche, CNR-IFN, Bari, Italy. [8]These authors contributed equally: Marco Piccardo, Benedikt Schwarz.. ✉e-mail: piccardo@g.harvard.edu; capasso@seas.harvard.edu

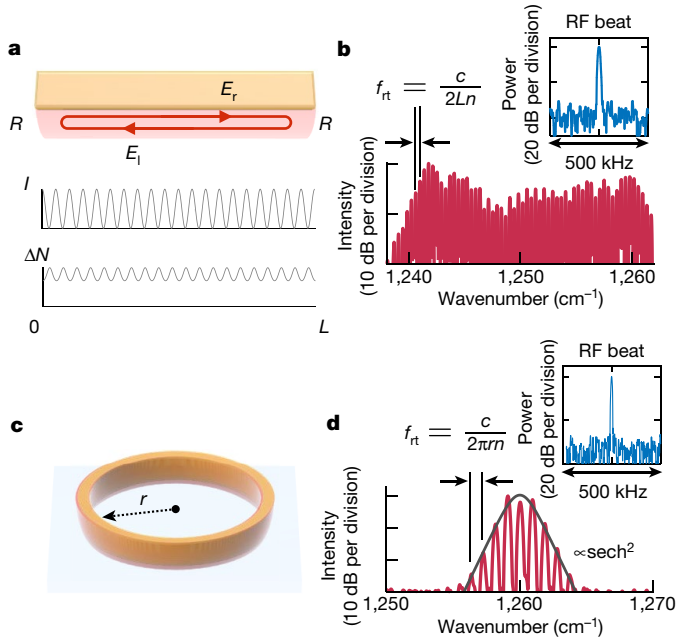


**Fig. 1 | Fabry–Pérot and ring frequency combs. a**, Schematic of a Fabry–Pérot cavity with rightward ($E_r$) and leftward ($E_l$) propagating waves coupled through facets of reflectivity $R$. As a result of the counterpropagating waves, optical standing waves of intensity $I$ and a static grating of population inversion $\Delta N$ are formed in the cavity of length $L$. **b**, Experimental optical spectrum of a Fabry–Pérot frequency comb generated from a QCL ($L$ = 3.7 mm). The round-trip frequency ($f_{rt}$) defines the comb spacing (11.5 GHz), which is shown in the inset. **c**, Schematic of a monolithic semiconductor ring laser of radius $r$. **d**, Experimental optical spectrum of a ring QCL frequency comb ($r$ = 500 μm). The envelope of the spectrum is fitted to a sech$^2$ function for the discussion on solitonic structures. Also shown is the narrow electrical beat note of the laser (central frequency 27.8 GHz). The two lasers are fabricated from the same material. The resolution of the optical spectrum analyser is 3 GHz in **b** and 6 GHz in **d**, and the resolution bandwidth of the radiofrequency (RF) spectrum analyser is 9.1 kHz in **b** and 5.6 kHz in **d**.

combine nonlinearity and gain[10] and have applications in dual-comb spectroscopy[24], metrology[25] and microwave photonics[26]. QCL frequency combs typically have the Fabry–Pérot geometry (Fig. 1a) and serve the mid-infrared and terahertz regions of the electromagnetic spectrum, which are strategic for chemical sensing. They have the advantages of broad tunability, through band-structure engineering, and high portability because they are electrically pumped and compact. Here we fabricate ring QCLs in a ridge waveguide geometry (Fig. 1c). These ring QLCs emit in the mid-infrared and operate at room temperature under constant electrical injection (Methods). A small fraction of light can escape from the ring cavity owing to scattering, allowing us to perform a spectral characterization.

We find that at an injection level only fractionally higher than the lasing threshold $J_{th}$ (typically $1.1J_{th}$–$1.5J_{th}$), the ring lasers undergo a transition to a multimode regime (Fig. 1d) that is distinctly different from those observed in Fabry–Pérot QCLs (Fig. 1b). The optical spectrum of the ring has fewer modes and exhibits a bell-shaped envelope. As in Fabry–Pérot resonators, the modes are separated by the round-trip frequency of the cavity $f_{rt} = c/(2\pi rn)$, where $r$ is the ring radius, $n$ = 3.4 is the effective refractive index of the waveguide and $c$ is the speed of light in vacuum. The coherence of the state is manifested by its narrow beat note (Supplementary Fig. 2), which indicates its frequency comb nature, further confirmed by a coherent beat note detection technique (Extended Data Fig. 1). A notable feature of the instability is that as the current in the device is increased, the laser can revert back to single-mode operation (Extended Data Fig. 2)—a feature not observed in regular Fabry–Pérot lasers. A multimode instability close to the threshold has been reported also for a ring dye laser[27] but with different features, namely, suppression of the resonant mode and a parametric gain of two side modes separated by about the Rabi frequency.

## Ginzburg–Landau theory

To support the experimental evidence of multimode operation, we reexamine the theory of lasers with fast gain media. We show that ring frequency combs can be explained on the basis of a phase instability that affects the single-mode solution of the complex Ginzburg–Landau equation (CGLE)[11,28]. The CGLE is a nonlinear differential equation that describes spatially extended systems of coupled nonlinear oscillators. It appears in many branches of physics, such as superconductivity, Bose–Einstein condensation and quantum field theory. In semiconductor laser theory, it can be shown that the field dynamics is described by a CGLE assuming fast gain relaxation[29]. Although fast relaxation is not applicable to a conventional bipolar semiconductor laser (diode laser), it is a well known property of QCLs. From the master equation of lasers with fast gain media[20] we derive the CGLE for the laser field $E$:

$$\partial_t E = E + (1 + ic_D)\partial_z^2 E - (1 + ic_{NL})|E|^2 E \quad (1)$$

where $t$ is the time and $z$ is the spatial coordinate running along the ring cavity (see Supplementary Information for the analytical derivation). The only two parameters of the equation are $c_D$ and $c_{NL}$, which control the stability of the system and relate to dispersive and nonlinear effects, respectively. In the case of QCLs, $c_D$ depends on the group velocity dispersion (GVD), and $c_{NL}$ depends on the Kerr coefficient. Although the bulk Kerr nonlinearity of a semiconductor crystal is small, its contribution is compensated by a term of the same order given by the linewidth enhancement factor (LEF)[12,20]. Despite its different nature from the Kerr nonlinearity, the LEF enters both the $c_D$ and $c_{NL}$ terms and provides the phase-amplitude coupling needed for the phase instability.

In CGLE theory, the parameter space spun by $c_D$ and $c_{NL}$ is divided into different stability regions by the Benjamin–Feir lines[11,30], which are defined by $1 + c_D c_{NL} = 0$. The inner region confined by the lines has stable, purely single-mode solutions, whereas the solutions lying in the two outer regions exhibit a phase instability[29], which makes them multimode. We investigate the spectral content of the laser field solutions according to their location in the CGLE parameter space. In Fig. 2a we show the result of space–time domain simulations of a ring QCL for different points in the ($c_D$, $c_{NL}$) parameter space determined by typical laser parameters (Extended Data Table 1). In these numerical simulations we use the full laser model without approximations[20], and the CGLE is used only to guide the choice of laser parameters, allowing us to probe solutions in various points of the parameter space. The computed optical spectra confirm that in the stable region (white) only single-mode solutions are supported, whereas in the instability regions (red) the laser attains a multimode regime despite the absence of SHB, as already suggested by a recent theory of ring QCLs based on the effective Maxwell–Bloch equations[31]. The ($c_D$, $c_{NL}$) coordinates corresponding to our laser parameters, as obtained from the GVD and LEF measurements (Fig. 2c, d), are marked in Fig. 2a and show that the experimentally observed multimode instability is compatible with the phase turbulence mechanism.

## Emergence of order from turbulence

Space–time simulations allow us to resolve the full temporal evolution of the laser (Fig. 2b, Supplementary Video). Starting from spontaneous emission, discontinuous changes of the laser field are produced. Amplitude fluctuations of the first lasing mode are coupled to phase fluctuations via the LEF or $\alpha$ parameter $\alpha = (\partial n'/\partial N)/(\partial n''/\partial N)$, where $n'$ and $n''$ are the real and imaginary parts of the refractive index, respectively, and $N$ is the carrier density[12]. Physically, fluctuations of $n'$ in the QCL active region lead to fluctuations in the spacing between the lasing

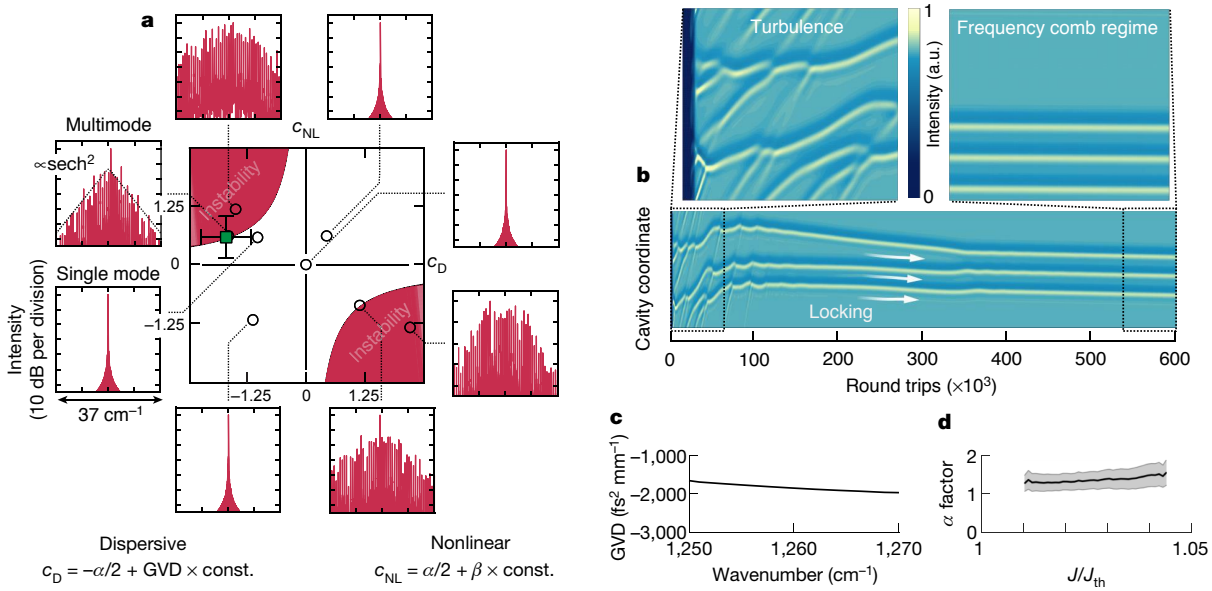


**Fig. 2 | Conditions for the phase instability in a monolithic ring laser.** **a**, Theoretical spectra obtained by solving the laser master equation are shown for different points in parameter space, confirming the behaviour expected from Ginzburg–Landau theory. In the simulations, SHB is turned off, so the obtained multimode regimes are due to the Ginzburg–Landau phase instability. In all plots the *x* axis spans 50 longitudinal modes of the ring and the *y* axis shows intensity (10 dB per division). Also shown is the region corresponding to the experimental devices, as obtained from the laser parameters, with the related uncertainties corresponding to the standard deviation (square marker; Supplementary Table 1). In the simulated spectrum corresponding to this point, a sech² envelope was fitted to the envelope for the purposes of the discussion on solitonic structures (dashed line). The formulas shown in the inset are an approximation in the limit of small linewidth-enhancement factors (Supplementary Information). GVD is the group velocity dispersion, $\alpha$ is the linewidth enhancement factor and $\beta$ is the Kerr nonlinearity, which is small in QCLs. **b**, Space–time simulation of the laser dynamics, showing the intensity in the ring cavity at every round trip. Starting from spontaneous emission (dark stripe in the left inset), the laser destabilizes into a turbulent regime and eventually reaches a frequency comb regime. The simulation solves the laser master equation for 600 million time steps (0.05 ms interval). The corresponding point in parameter space is indicated by the square marker in **a**. **c**, **d**, Measurement of two physical quantities entering $c_D$ and $c_{NL}$ for a ring QCL. In **d**, the experimental values are shown as a function of current density normalized to the lasing threshold. Error bars are obtained as the standard deviation of multiple (20) repeated measurements. a.u., arbitrary units.

mode and the side modes. The shifts of the latter with respect to the gain peak eventually lead to multimode lasing, despite the absence of SHB. In CGLE theory, the resulting dynamical behaviour shown in Fig. 2b is described as 'phase turbulence'. This regime is characterized by the presence of chaotic intensity fluctuations with small amplitude that never reach zero and by the absence of phase dislocations[32] (for a detailed discussion of the role of turbulence, see Supplementary Information). After a relatively long time interval (about 400,000 round trips) the laser reaches a frequency comb regime, where the intensity becomes periodic, with the waveform repeating itself at every round trip. Whereas phase turbulence provides a coupling mechanism among the modes via the LEF, which is alternative to SHB in Fabry–Pérot lasers, it is the semiconductor saturation nonlinearity via four-wave mixing that, for a sufficiently high intracavity field, becomes efficient at compensating dispersion through a self-injection mechanism[10]. Besides the conventional description in terms of LEF and GVD[20], the formation of the frequency comb can be described from the point of view of Ginzburg–Landau theory as the morphogenesis of a regular spatiotemporal pattern. Here the locking process manifests itself as the interaction of confined intensity structures that shift with respect to each other, eventually conforming into a single stable structure (Fig. 2b).

### Role of intracavity defects

In demonstrating that phase turbulence lies at the heart of the multimode instability of ring lasers, it is essential to distinguish it from another mechanism that normally drives the instability, SHB. Here we show that in a ring cavity that supports SHB, the multimode instability leads to a completely different comb state. SHB arises in a cavity in the presence of a well defined reflection point that couples counterpropagating waves. Whereas in a Fabry–Pérot cavity the waves are naturally coupled owing to reflections off the cleaved facets, in a ring cavity an analogous reflection point—a defect—must be intentionally introduced. This is because unintentional defects, which may result from imperfections in fabrication, are insufficient to trigger the SHB instability (Supplementary Fig. 5). We embed a defect in a ring laser waveguide by means of focused ion beam lithography (Fig. 3a). A simple, yet effective, way of controlling the defect reflectivity is to etch a narrow slit across the waveguide to create an air gap in the active region of the laser (Fig. 3b). We choose a slit width of 0.5 µm that gives a reflectivity of $R \approx 22\%$, which is close to the facet reflectivity of an uncoated Fabry–Pérot QCL ($R = 29\%$). The defect-engineered laser generates a frequency comb with a spectrum that is drastically different from that of a ring without an intentional defect (Fig. 3c, Supplementary Fig. 6). The spectrum has an irregular envelope—the result of complex laser mode competition—similar to that of Fabry–Pérot devices, in which multimode operation is also dominated by SHB. The presence of optical standing waves enabling SHB is demonstrated by the beat note pattern measured along the cavity, with a maximum located, as expected, at the engineered defect (Fig. 3d, Extended Data Fig. 3, Supplementary Fig. 3). Space–time simulations of this laser confirm a different dynamics from that of non-defect-engineered rings. The instability shows large intensity fluctuations and a fragmented temporal evolution (Fig. 3e). Locking occurs over a shorter time interval (about 10,000 round trips) and results in a nearly flat intensity waveform, as in Fabry–Pérot QCL combs[20]. These results show that high reflectivity values, comparable to those of uncoated Fabry–Pérot resonators, are needed to mask the effects of phase turbulence in a ring and enable multimode emission due to SHB.

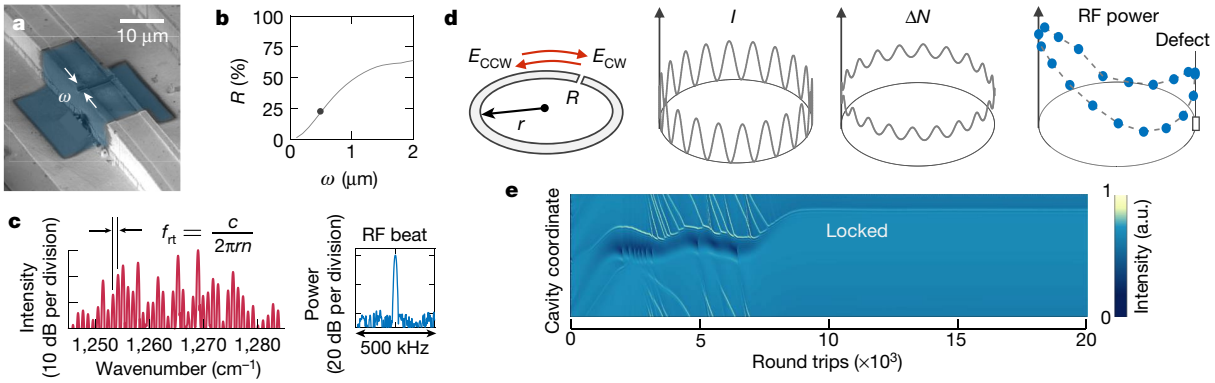


**Fig. 3 | Defect-engineered ring frequency comb. a**, Scanning electron microscope image of the defect-engineered ring laser, showing the aperture in the metal (blue region in false colour) with a slit width of $\omega = 0.5$ μm fabricated by focused ion beam lithography. **b**, Reflectivity induced by the slit as a function of its width, as calculated from numerical wave simulations (solid line). The reflectivity of the studied device is $R \approx 22\%$ (dot). **c**, Experimental optical spectrum of a defect-engineered ring QCL ($r = 500$ μm) fabricated from the same material as the other devices studied in this work. Also shown is the microwave beat note extracted from the laser (central frequency 27.8 GHz, resolution bandwidth 9.1 kHz). **d**, Schematic of a ring laser with an embedded engineered defect of reflectivity $R$. The defect induces clockwise ($E_{CW}$) and counterclockwise ($E_{CCW}$) waves, resulting in an optical standing wave of intensity $I$ and a static population grating of population inversion $\Delta N$. The right panel shows the experimental beat note power pattern (RF power) measured along the perimeter of the ring at the round-trip frequency indicating a bidirectional regime. **e**, Space–time simulation of a ring laser with a defect ($R = 25\%$).

## Discussion

Linking the physics of ring lasers to the CGLE suggests a connection with Kerr-driven frequency comb generators. The latter are usually described by the Lugiato–Lefever equation[13] (LLE) with well known soliton solutions[33–36] derived from the CGLE with coherent forcing in the limit of large $c_D$ and $c_{NL}$ parameters. Moreover, we showed that the LEF, which enters both Ginzburg–Landau parameters in the case of a ring laser, adds up to the contributions of the Kerr nonlinearity and the GVD. The interplay of dispersive and nonlinear effects is essential to produce a self-starting instability, as in the case of the modulation instability that lies at the origin of Kerr solitons in microresonators[36].

The link with Kerr combs can be seen not only in the governing equations but also from the optical spectra. The bell-shaped envelope of the QCL ring comb spectra fits well to a $\mathrm{sech}^2$ function (Figs. 1d, 2a), which is characteristic of dissipative Kerr solitons. The observation of spectral gaps in certain devices (Extended Data Figs. 2, 4) is also reminiscent of the variety of Kerr soliton spectra measured for different pump detuning conditions[33,34]. These observations indicate that the necessary conditions for the formation of solitonic structures[31] exist in ring QCLs, although proving their occurrence is a considerable experimental and theoretical undertaking that requires further investigation. It is known from Ginzburg–Landau theory that the CGLE can have localized structures, such as 'modulation amplitude waves'[37], as solutions, similarly to the LLE. These appear in the phase turbulence regime and exhibit weak amplitude modulations on a homogeneous background—features also observed in our numerical simulations of ring QCLs (Fig. 2b, Supplementary Fig. 1) and supported by the experimental characterization of the spectral phases of these lasers (Supplementary Information). In the simulations we find that the number of structures in states such as that shown in Fig. 2b vary stochastically with the initial conditions of the laser; by changing only the seed of the spontaneous emission noise and repeating the same simulation, we obtained a laser state with four structures instead of three (Extended Data Fig. 1). This is a clear indication of a multistability phenomenon, which is typical of dissipative solitons in extended systems such as Kerr microcombs.

We also highlight a historical analogy with the progress in the field of passive microresonators: prior theoretical studies by Lugiato and co-workers on transverse patterns in lasers[38,39], temporally contiguous with the well known work with Lefever on transverse patterns in passive optical systems[13], derived an equation with a mathematical form very similar to our CGLE, which however describes longitudinal patterns in ring lasers. This is reminiscent of the history of microresonators, in which the LLE anticipated the first experimental demonstration of Kerr combs[40], which also have longitudinal patterns and were later traced back to the LLE.

Besides the several analogies between the two classes of localized structures/combs in Kerr microresonators and ring QCLs highlighted so far, we believe that there exist a few fundamental differences that could imply different solitonic properties (for example, response to external addressing, mutual interaction), but the exhaustive study of which would require a dedicated future work. These mainly originate from the different kinds of nonlinearity providing the phase locking between competing modes and the absence of a forcing field in ring QCLs, which might give an advantage to these devices in terms of compactness. In fact, whereas the pumping of passive microresonators requires energy incoming through optical injection, which is responsible for the appearance of a strong central mode in the comb spectrum that is undesirable in many applications, QCL combs operate without an injected field. In this regard, QCLs are more similar to the recently demonstrated laser cavity–soliton microcombs[41]—Kerr microcavities nested in an amplifying fibre loop providing gain—but are more compact. A ring QCL acting as an electrically pumped microresonator would hold a substantial technological potential, in particular considering the strategic spectral ranges covered by QCLs. Further improvements in this direction should concentrate on the design of efficient light outcouplers—with the precaution of not perturbing the physics of the phase turbulence instability—and on the extension of the comb bandwidth that, unlike the case of Fabry–Pérot QCLs, is not limited by SHB, but only by the LEF and GVD.

## Online content

Any methods, additional references, Nature Research reporting summaries, source data, extended data, supplementary information, acknowledgements, peer review information; details of author contributions and competing interests; and statements of data and code availability are available at https://doi.org/10.1038/s41586-020-2386-6.

1. Reynolds, O. XXIX. An experimental investigation of the circumstances which determine whether the motion of water shall be direct or sinuous, and of the law of resistance in parallel channels. *Philos. Trans. R. Soc. Lond.* **174**, 935–982 (1883).
2. Hänsch, T. W. Nobel lecture: passion for precision. *Rev. Mod. Phys.* **78**, 1297–1309 (2006).
3. Udem, T., Holzwarth, R. & Hänsch, T. W. Optical frequency metrology. *Nature* **416**, 233–237 (2002).
4. Picqué, N. & Hänsch, T. W. Frequency comb spectroscopy. *Nat. Photon.* **13**, 146–157 (2019).
5. Vahala, K. J. Optical microcavities. *Nature* **424**, 839–846 (2003).
6. Gaeta, A. L., Lipson, M. & Kippenberg, T. J. Photonic-chip-based frequency combs. *Nat. Photon.* **13**, 158–169 (2019).
7. Risken, H. & Nummedal, K. Self-pulsing in lasers. *J. Appl. Phys.* **39**, 4662–4672 (1968).
8. Graham, R. & Haken, H. Quantum theory of light propagation in a fluctuating laser-active medium. *Z. Phys.* **213**, 420–450 (1968).
9. Mujagić, E. et al. Grating-coupled surface emitting quantum cascade ring lasers. *Appl. Phys. Lett.* **93**, 011108 (2008).
10. Hugi, A., Villares, G., Blaser, S., Liu, H. C. & Faist, J. Mid-infrared frequency comb based on a quantum cascade laser. *Nature* **492**, 229–233 (2012).
11. Aranson, I. S. & Kramer, L. The world of the complex Ginzburg–Landau equation. *Rev. Mod. Phys.* **74**, 99–143 (2002).
12. Henry, C. Theory of the linewidth of semiconductor lasers. *IEEE J. Quantum Electron.* **18**, 259–264 (1982).
13. Lugiato, L. A. & Lefever, R. Spatial dissipative structures in passive optical systems. *Phys. Rev. Lett.* **58**, 2209–2211 (1987).
14. Kues, M. et al. Quantum optical microcombs. *Nat. Photon.* **13**, 170–179 (2019).
15. Kippenberg, T. J., Holzwarth, R. & Diddams, S. A. Microresonator-based optical frequency combs. *Science* **332**, 555–559 (2011).
16. Herr, T. et al. Universal formation dynamics and noise of Kerr-frequency combs in microresonators. *Nat. Photon.* **6**, 480–487 (2012).
17. Agrawal, G. P. Population pulsations and nondegenerate four-wave mixing in semiconductor lasers and amplifiers. *J. Opt. Soc. Am. B* **5**, 147–159 (1988).
18. Faist, J. et al. Quantum cascade laser frequency combs. *Nanophotonics* **5**, 272–291 (2016).
19. Piccardo, M. et al. The harmonic state of quantum cascade lasers: origin, control, and prospective applications. *Opt. Express* **26**, 9464–9483 (2018).
20. Opačak, N. & Schwarz, B. Theory of frequency-modulated combs in lasers with spatial hole burning, dispersion, and Kerr nonlinearity. *Phys. Rev. Lett.* **123**, 243902 (2019).
21. Matsumoto, N. & Kumabe, K. AlGaAs-GaAs semiconductor ring laser. *Jpn. J. Appl. Phys.* **16**, 1395–1398 (1977).
22. Krauss, T., Laybourn, P. J. R. & Roberts, J. CW operation of semiconductor ring lasers. *Electron. Lett.* **26**, 2095–2097 (1990).
23. Gelens, L. et al. Exploring multistability in semiconductor ring lasers: theory and experiment. *Phys. Rev. Lett.* **102**, 193904 (2009).
24. Villares, G., Hugi, A., Blaser, S. & Faist, J. Dual-comb spectroscopy based on quantum-cascade-laser frequency combs. *Nat. Commun.* **5**, 5192 (2014).
25. Consolino, L. et al. Fully phase-stabilized quantum cascade laser frequency comb. *Nat. Commun.* **10**, 2938 (2019).
26. Piccardo, M. et al. Radio frequency transmitter based on a laser frequency comb. *Proc. Natl Acad. Sci. USA* **116**, 9181–9185 (2019); correction **116** 17598 (2019).
27. Hillman, L. W., Krasiński, J., Boyd, R. W. & Stroud, C. R. Observation of higher order dynamical states of a homogeneously broadened laser. *Phys. Rev. Lett.* **52**, 1605–1608 (1984).
28. Staliunas, K. Laser Ginzburg–Landau equation and laser hydrodynamics. *Phys. Rev. A* **48**, 1573–1581 (1993).
29. Gil, L. & Lippi, G. L. Phase instability in semiconductor lasers. *Phys. Rev. Lett.* **113**, 213902 (2014).
30. Chate, H. Spatiotemporal intermittency regimes of the one-dimensional complex Ginzburg–Landau equation. *Nonlinearity* **7**, 185–204 (1994).
31. Columbo, L. L., Barbieri, S., Sirtori, C. & Brambilla, M. Dynamics of a broad-band quantum cascade laser: from chaos to coherent dynamics and mode-locking. *Opt. Express* **26**, 2829–2847 (2018).
32. Shraiman, B. et al. Spatiotemporal chaos in the one-dimensional complex Ginzburg–Landau equation. *Physica D* **57**, 241–248 (1992).
33. Kippenberg, T. J., Gaeta, A. L., Lipson, M. & Gorodetsky, M. L. Dissipative Kerr solitons in optical microresonators. *Science* **361**, eaan8083 (2018).
34. Herr, T. et al. Temporal solitons in optical microresonators. *Nat. Photon.* **8**, 145–152 (2014).
35. Cole, D. C., Lamb, E. S., Del'Haye, P., Diddams, S. A. & Papp, S. B. Soliton crystals in Kerr resonators. *Nat. Photon.* **11**, 671–676 (2017).
36. Karpov, M. et al. Dynamics of soliton crystals in optical microresonators. *Nat. Phys.* **15**, 1071–1077 (2019).
37. Brusch, L., Zimmermann, M. G., van Hecke, M., Bär, M. & Torcini, A. Modulated amplitude waves and the transition from phase to defect chaos. *Phys. Rev. Lett.* **85**, 86–89 (2000).
38. Lugiato, L. A., Oldano, C. & Narducci, L. M. Cooperative frequency locking and stationary spatial structures in lasers. *J. Opt. Soc. Am. B* **5**, 879–888 (1988).
39. Kaige, W., Abraham, N. B. & Lugiato, L. A. Leading role of optical phase instabilities in the formation of certain laser transverse patterns. *Phys. Rev. A* **47**, 1263–1273 (1993).
40. Del'Haye, P. et al. Optical frequency comb generation from a monolithic microresonator. *Nature* **450**, 1214–1217 (2007).
41. Bao, H. et al. Laser cavity-soliton microcombs. *Nat. Photon.* **13**, 384–389 (2019).

# Methods

### QCLs

The lasers emit at around 8 μm and have a structure consisting of GaInAs/AlInAs layers on an InP substrate. The waveguide width is 10 μm and the inner radius $r$ is 500 μm or 600 μm (Supplementary Fig. 11). The active region consists of AlInAs/GaInAs/InP layers and the band structure design is based on a single-phonon continuum depopulation scheme[42]. The lasers are operated under constant electrical injection with a low-noise current driver (Wavelength Electronics QCL LAB1500), and their temperature is stabilized at 16 °C using a low-thermal-drift temperature controller (Wavelength Electronics TC5). The threshold current density of a symmetric ring is observed to be as low as 1.1 kA cm$^{-2}$, and that of the defect-engineered ring is 1.3 kA cm$^{-2}$. The increase in threshold current density in the defect-engineered ring is attributed to the losses induced by the defect. For comparison, the threshold current density of a Fabry–Pérot device fabricated from the same material, with the same waveguide width and cleaved to have a symmetric ring of approximately the same length ($L$ = 3.7 mm) is 1.4 kA cm$^{-2}$. Only a small amount of light (≲1 mW) scatters out of the ring waveguide, minimizing the perturbations caused by outcoupling on the intrinsic states of the lasers. The laser spectral output is measured using a Fourier transform infrared spectrometer and a sensitive photodetector (HgCdTe detector cooled at 77 K). Beat notes produced during the operation of the frequency comb are electrically extracted from the laser chip using a radiofrequency probe connected to a spectrum analyser and exhibit a narrow (sub-kilohertz) linewidth. The symmetry of the optical spectra of the ring combs is a further indication of the coherence of these states. The suppression of the central optical mode, which can be observed in certain devices (Extended Data Fig. 5), is a signature of a parametric process and resembles the spectra of frequency-modulated combs. Because the GVD and LEF characterizations rely on techniques[43–46] for which the output power from a ring would be insufficient, we measure these quantities using Fabry–Pérot devices fabricated from the same material and having the same waveguide width as the rings (10 μm). More details on the LEF characterization are given in Supplementary Information (Supplementary Figs. 7–10). Other works investigating QCL cavities with a circular geometry are described in refs. [9,47–54].

### Numerical simulations

The theory presented in this work is backed up by numerical simulations that are based on the laser master equation. This was derived in ref. [20] starting from the full Maxwell–Bloch system of equations. This enables a considerable increase in implementation efficiency compared to the full Maxwell–Bloch system while maintaining the fidelity of the model in the case of a fast gain medium, such as QCLs. To further improve the calculation speed, the code is highly parallelized and implemented in a CUDA platform, called from a Python C++ extension interface. The calculations are conducted on a graphics processing unit (GPU) within a PC, which allows extremely short computation times compared to a standard code implementation on a central processing unit (CPU). We used an NVIDIA GeForce GTX 1070 Ti GPU, which resulted in a speed-up factor of 500 compared to the CPU implementation. As an example, the space–time simulation shown in Fig. 2b, which consists of 600 million time steps, took 27 min to run.

### Defect engineering

We use focused ion beam milling to engineer defects in ring QCLs. Focused ion beam lithography is a maskless dry-etching technique originally developed for the repair of photolithography masks and for the preparation of samples for transmission electron microscopy. The writing settings for the rectangular pattern are 0.6 × 10 μm$^2$ with a depth setting of 1.43 μm. The actual width of the slit cut by the focused ion beam (FEI Helios 660) across the ring waveguide is 500 nm. The dwell time is 1 μs and the current is 0.43 nA. The recipe is finely tuned to avoid the devastating effects of $Ga^+$ ions getting implanted in the QCL layers, effectively creating a current leakage path of high resistance that burns during laser operation[55]. We also toned to account for the systematic spatial shifts between the written patterns and the location of the focus of the beam. The reflectivity of the defect is calculated using the frequency-domain electromagnetic wave model (*emw* module) of COMSOL. We confirm the values of the defect reflectivity obtained from COMSOL simulations with a calculation using the transfer matrix formalism for a dielectric–air–dielectric interface. The reflectivity peak corresponds to a defect width of approximately a quarter wavelength in air (about 2 μm), and its value (64%) is dictated by the air–dielectric index contrast. If needed, higher reflectivity values could be achieved by defining a distributed Bragg reflector section in the waveguide using focused ion beam milling.

### Radiofrequency gratings

For the measurement of the radiofrequency (or dynamic) gratings we use a coaxial radiofrequency probe (Quater A-20338) mounted on an XYZ micrometer positioning stage and placed in contact with the top electrode of the rings. The scanning probe is manually positioned along the perimeter of the ring laser cavity[56] (Supplementary Fig. 4). The signal from the probe at every position is amplified with a radiofrequency amplifier (CTT ALN 300–8023, bandwidth 18–26.5 GHz, gain 22 dB) and recorded with a spectrum analyser (Agilent E4448A). The specified 3-dB bandwidth of the probe (d.c. 18 GHz) is smaller than the typical beat note frequency of the ring lasers (23–27 GHz); however, the extracted radiofrequency signal is still sufficient to characterize the beat note power distribution along the ring cavity.

## Data availability

Source data for Figs. 1–3 are provided with the paper. Additional data that support the findings of this study are available from the corresponding authors upon reasonable request.

## Code availability

The codes used to plot the Benjamin–Feir space and related datasets, to calculate the Ginzburg–Landau $c_D$ and $c_{NL}$ parameters with error propagation, and to simulate the dynamic microwave gratings are available at: https://figshare.com/articles/Codes_for_Benjamin-Feir_space_parameters_and_dynamic_QCL_gratings/11967552/1; https://figshare.com/articles/Plot_code_and_datasets_for_phase_turbulence_space-time_plots/11967756/1; https://figshare.com/articles/Plot_code_and_datasets_for_defect_engineered_laser_space-time_plots/11967828/1. Information on the code developed to simulate the QCL dynamics and its results are available from the corresponding authors upon reasonable request.


42. Wang, C. A. et al. MOVPE growth of LWIR AlInAs/GaInAs/InP quantum cascade lasers: impact of growth and material quality on laser performance. *IEEE J. Sel. Top. Quantum Electron.* **23**, 1–13 (2017).
43. Hofstetter, D. & Faist, J. Measurement of semiconductor laser gain and dispersion curves utilizing Fourier transforms of the emission spectra. *IEEE Photonics Technol. Lett.* **11**, 1372–1374 (1999).
44. von Staden, J., Gensty, T., Elsäßer, W., Giuliani, G. & Mann, C. Measurements of the *α* factor of a distributed-feedback quantum cascade laser by an optical feedback self-mixing technique. *Opt. Lett.* **31**, 2574–2576 (2006).
45. Jumpertz, L. et al. Measurements of the linewidth enhancement factor of mid-infrared quantum cascade lasers by different optical feedback techniques. *AIP Adv.* **6**, 015212 (2016).
46. Kumazaki, N. et al. Spectral behavior of linewidth enhancement factor of a mid-infrared quantum cascade laser. *Jpn. J. Appl. Phys.* **47**, 6320–6326 (2008).
47. Szedlak, R. et al. Ring quantum cascade lasers with twisted wavefronts. *Sci. Rep.* **8**, 7998 (2018).
48. Malara, P. et al. External ring-cavity quantum cascade lasers. *Appl. Phys. Lett.* **102**, 141105 (2013).
49. Wojcik, A. K. et al. Generation of picosecond pulses and frequency combs in actively mode locked external ring cavity quantum cascade lasers. *Appl. Phys. Lett.* **103**, 231102 (2013).

50. Revin, D. G., Hemingway, M., Wang, Y., Cockburn, J. W. & Belyanin, A. Active mode locking of quantum cascade lasers in an external ring cavity. *Nat. Commun*. **7**, 11440 (2016).
51. Faist, J. et al. Quantum cascade disk lasers. *Appl. Phys. Lett*. **69**, 2456–2458 (1996).
52. Meng, B. et al. Mid-infrared frequency comb from a ring quantum cascade laser. *Optica* **7**, 162–167 (2020).
53. Gmachl, C. et al. High-power directional emission from microlasers with chaotic resonators. *Science* **280**, 1556–1564 (1998).
54. Wang, Q. J. et al. Whispering-gallery mode resonators for highly unidirectional laser action. *Proc. Natl Acad. Sci. USA* **107**, 22407–22412 (2010).
55. Lončar, M. et al. Design and fabrication of photonic crystal quantum cascade lasers for optofluidics. *Opt. Express* **15**, 4499–4514 (2007).
56. Piccardo, M. et al. Time-dependent population inversion gratings in laser frequency combs. *Optica* **5**, 475–478 (2018).

**Acknowledgements** We acknowledge support from the National Science Foundation under award numbers ECCS-1614631 and CCSS-1807323. Any opinions, findings, conclusions or recommendations expressed in this material are those of the authors and do not necessarily reflect the views of the National Science Foundation. This work was performed in part at the Center for Nanoscale Systems (CNS), a member of the National Nanotechnology Coordinated Infrastructure Network (NNCI), which is supported by the National Science Foundation under NSF award number 1541959. B.S. was supported by the Austrian Science Fund (FWF) within the project NanoPlas. We gratefully acknowledge C. A. Wang, M. K. Connors and D. McNulty for providing the QCL material. We thank V. Ginis, T. S. Mansuripur and F. Grillot for discussions, G. Strasser for enabling the device fabrication, P. Chevalier for cleaving the devices and the D. Ham group for lending us microwave amplifiers. We acknowledge discussions with L. A. Lugiato on spatial patterns in lasers and Kerr microcombs.

**Author contributions** M.P. initiated the project. B.S. and M.B. fabricated the devices. M.P, B.S., D.K., S.J. and J.H. carried out the experiments. M.P. derived the grating model. B.S. and N.O. derived the Ginzburg–Landau theory with suggestions from L.L.C. B.S., N.O. and Y.W. performed the laser space–time domain simulations. D.K., M.T., W.T.C. and A.Y.Z. performed the defect engineering based on simulations from M.P. and D.K. M.P. wrote most of the manuscript. M.P., N.O., D.K. and S.J. wrote sections of the Supplementary Information. A.B. and F.C. supervised the project. M.P., B.S., D.K., M.B., N.O., Y.W., S.J., L.L.C., A.B. and F.C. contributed to the analysis, discussion and writing of the paper.

**Competing interests** The authors declare no competing interests.

**Additional information**

**Supplementary information** is available for this paper at https://doi.org/10.1038/s41586-020-2386-6.
**Correspondence and requests for materials** should be addressed to M.P. or F.C.
**Peer review information** *Nature* thanks Roberto Morandotti, Johann Riemensberger and the other, anonymous, reviewer(s) for their contribution to the peer review of this work.
**Reprints and permissions information** is available at http://www.nature.com/reprints.

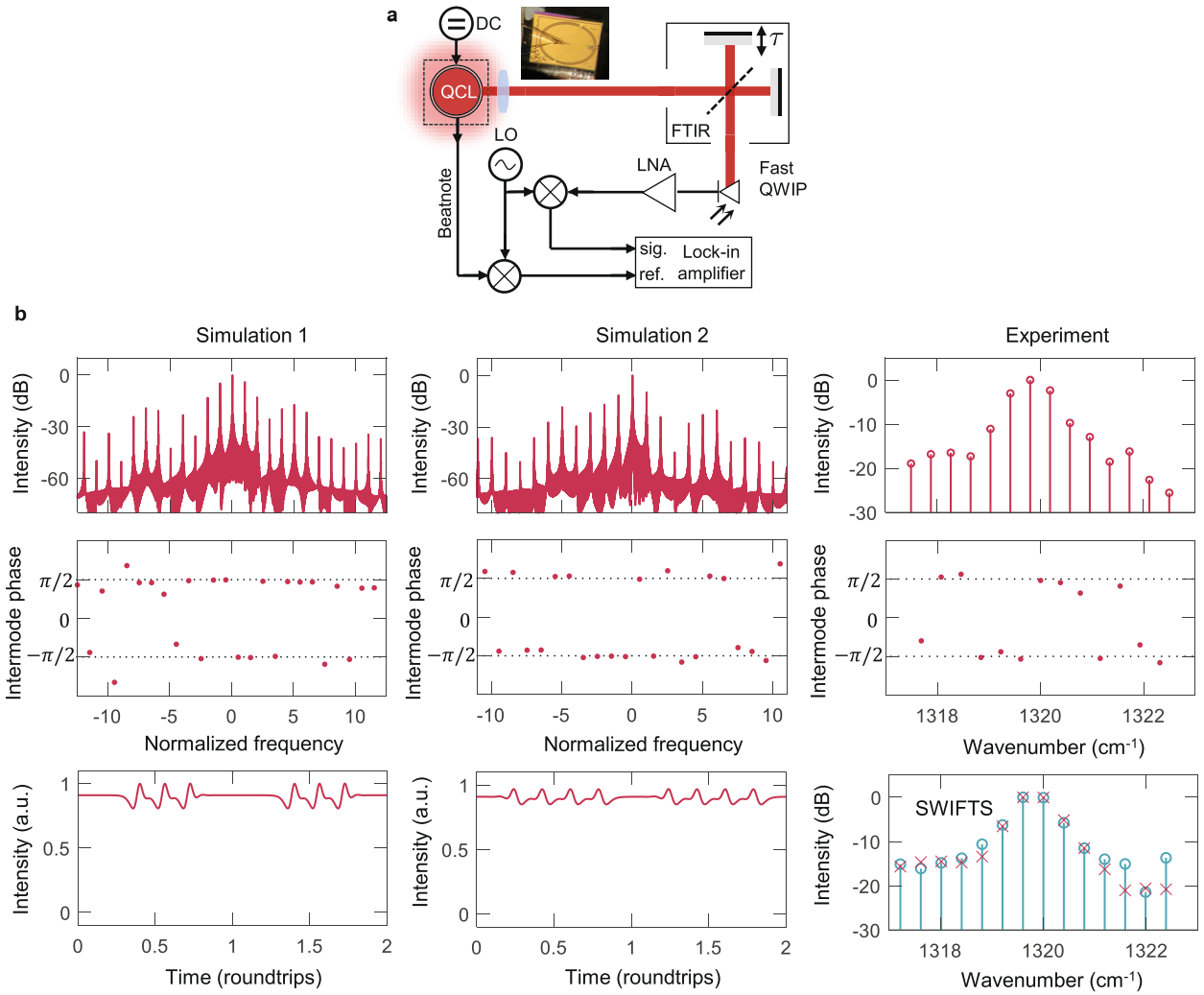


**Extended Data Fig. 1 | Coherence and phase of the ring frequency combs.** **a**, Schematic of the Shifted Wave Interference Fourier Transform Spectroscopy (SWIFTS) setup. The inset shows a microscope image of the QCL ring. LNA, low-noise amplifier; FTIR, Fourier transform infrared spectrometer; LO, local oscillator; QWIP, quantum well infrared photodetector. **b**, Comparison of the simulations with the experimental results obtained by SWIFTS. The displayed simulation results show the spectral amplitudes (top), the intermodal difference phases (middle) and the corresponding time-domain signals (bottom). Different seeds for spontaneous emission noise were used in the two simulations. The experimental data show the spectrum (top), the measured intermodal difference phases (middle) and the SWIFTS amplitudes (bottom). The red crosses on top of the SWIFTS amplitudes are given by $|A_n||A_{n-1}|$, that is, the geometric average of adjacent modes of the intensity spectrum. The red crosses agree well with the expected values for full phase coherence.

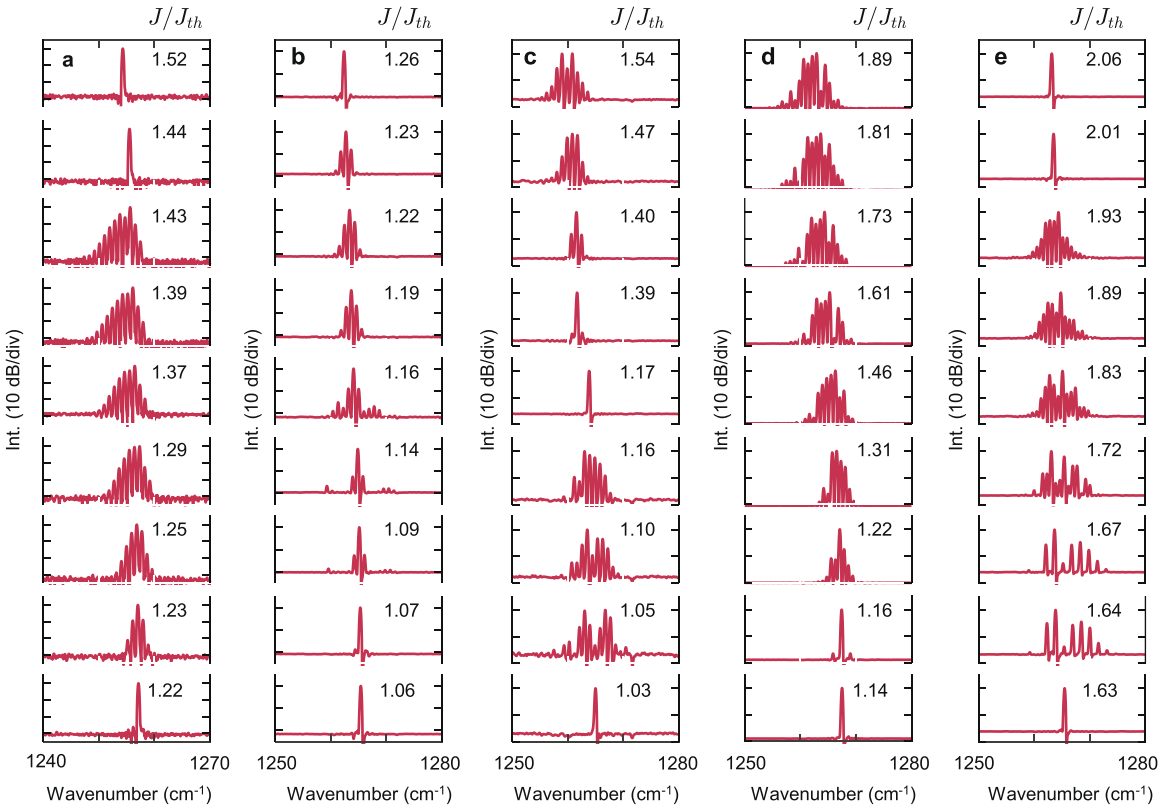


**Extended Data Fig. 2 | Evolution of the experimental optical spectra with injected current. a**–**e**, Spectral series corresponding to five distinct ring lasers. The multimode regime can switch on and off. The current density normalized to the lasing threshold is given to the right of each spectrum. Int., intensity.

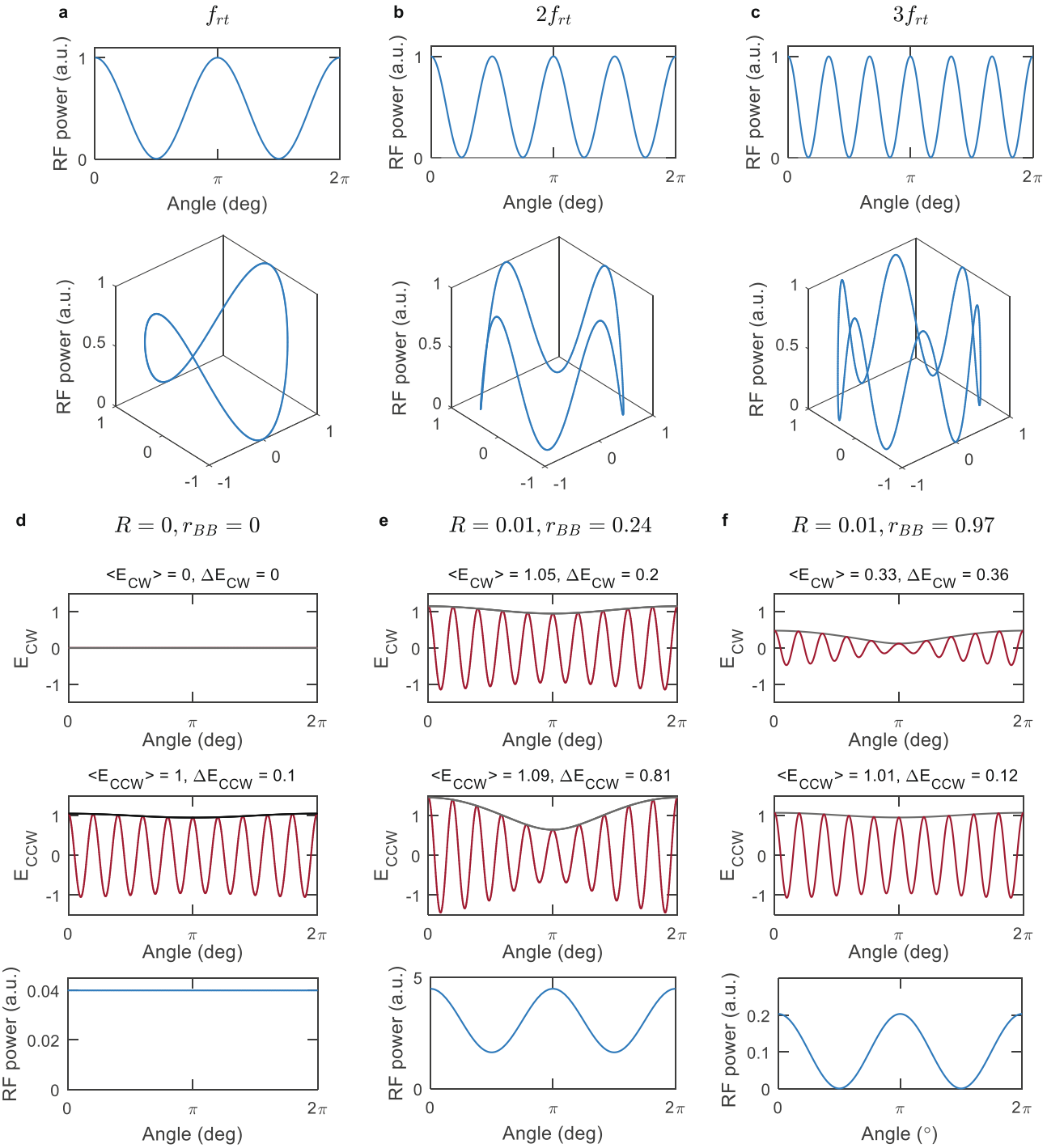


**Extended Data Fig. 3 | Dynamic gratings in ring lasers. a**–**c**, Beat patterns, calculated from the analytical model of a ring with a defect, that oscillate at the fundamental, second harmonic and third harmonic of the round-trip frequency $f_{rt}$. Patterns are shown both for the unwrapped angular coordinate (top) and as projected onto a two-dimensional ring (bottom). Here it is assumed that the counterpropagating optical beats have the same intensity. **d**–**f**, Different beat patterns calculated assuming various beat balance ratios $r_{BB}$, that is, different relative intensities of the counterpropagating optical beats, as discussed in the text. Also shown are the electric fields of the clockwise ($E_{CW}$) and counterclockwise ($E_{CCW}$) waves (red curves). The wavenumber is small for visual representation. The black lines correspond to the envelope of the fields, from which the mean values $\langle E \rangle$ and modulation amplitudes $\Delta E$ are calculated. The three cases correspond to: unidirectional lasing, which gives a uniform beat power across the cavity (**d**); bidirectional lasing with counterpropagating optical beats that are not fully balanced, which gives a beat grating with limited fringe visibility (**e**); bidirectional lasing with fully balanced optical beats, which gives a dynamic grating with strongly suppressed nodes (**f**).

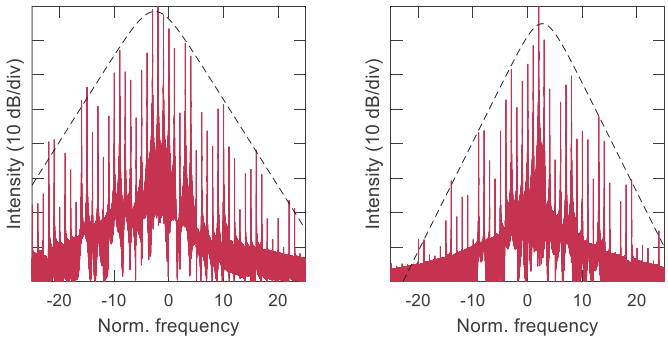


**Extended Data Fig. 4 | Spectral gaps.** Simulations of ring QCL states, showing spectral gaps reminiscent of multisoliton spectra in microresonators. A $\mathrm{sech}^2$ envelope is fitted to the dominant modes of the spectra. The simulations are carried out for slightly different initial conditions in terms of noise seed and GVD.

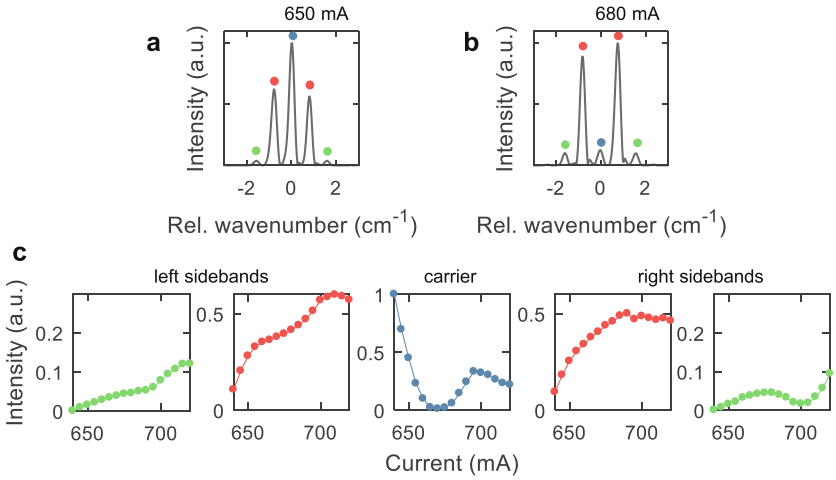


**Extended Data Fig. 5 | Central-mode suppression in ring spectra.** **a**, **b**, Experimental optical spectra of a ring frequency comb at two different pump currents, showing that the carrier (central mode) can become suppressed with respect to the first pair of sidebands. **c**, Pump-dependent evolution of the carrier and the first two pairs of sidebands. The colours of the series match the modes of the optical spectra.

**Extended Data Table 1 | Parameters used in the numerical simulations of QCLs**

| Symbol | Description | Value |
|---|---|---|
| $T_{ul}$ | Upper-lower level lifetime | 1 ps |
| $T_{ug}$ | Upper-ground level lifetime | 6 ps |
| $T_{lg}$ | Lower-ground level lifetime | 0.08 ps |
| $T_2$ | Dephasing time | 60 fs |
| $n$ | Refractive index | 3.3 |
| $D$ | Diffusion coefficient | 46 $cm^2/s$ |
| $\alpha_w$ | Waveguide power losses | 4 $cm^{-1}$ |
| $\mu$ | Dipole matrix element | 1 nm x e |
| $n_{tot}$ | Sheet density | 6 x $10^{10}$ $cm^{-2}$ |
| $\Gamma$ | Confinement factor | 1 |
| $L$ | Period length | 580 Å |
| $L_c$ | Cavity length | 4 mm |
| $\lambda_0$ | Central wavelength | 8 µm |